GSA Data Repository 2009272: The effects of flank collapses on volcano plumbing systems

Andrea Manconi, Marc-Antoine Longpré, Thomas R. Walter,
Valentin R. Troll and Thor H. Hansteen

The following supplementary material includes:

1. Details of magma density calculations procedures.
2. Details on construction of the finite element models and the assumed loading/unloading conditions.
3. Details on the effects of different melt percentages on elastic properties of the magmatic reservoir and on the effects of different magma reservoir shapes.
4. Details on limitations and the validity of the finite element models.
5. Discussion of the possible effects of mass-wasting on melt production beneath ocean island volcanoes.
6. Supplementary References.
7. Supplementary Tables and Figures:

   Table DR1: Sampling/outcrop localities, respective rock type and, where available, calculated density. Table DR2: Geometrical parameters used for the finite element simulations of the conical edifice and that of volcano flank collapse. Figure DR1: Effect of different melt% on the elastic properties of the storage zone. Figure DR2: Effect of shape of magma storage zone on decompression.

1. Magma density calculations procedures

Volcanic products of El Hierro were collected during two field campaigns and were subsequently analyzed for whole-rock and groundmass major element compositions. We estimated pre-eruptive magma densities for representative El Hierro samples (see Table DR1), following the procedure outlined by Spera (2000) and using initial volatile contents approximated on the basis of Dixon et al. (1997). That is, dissolved water contents were taken as $H_2O=3(P_2O_5)$ wt% and initial carbon dioxide as $CO_2=2(H_2O)$ by mass. El Hierro samples give a range of H_2O=1.4-4.0 wt% and CO_2=2.8-7.9 wt%, comparable to bulk volatile contents inferred by Dixon et al. (1997), for undegassed alkaline Hawaiian magmas. For the density calculations, we assumed f_{O2}=QFM+1, P=900 MPa (typical pressure of the main magma storage zone under Canarian shield volcanoes, see e.g. Klügel et al. 2005, Longpré et al. 2008 and Stroncik et al. 2008), and melts at their liquidus temperature, calculated using PETROLOG (Danyushevsky, 2001). The presence of phenocrysts in magma was also taken into account. For samples with <10 vol. % olivine + clinopyroxene, the density of the melt was taken as a reasonable approximation of the magma density. For samples with >10 vol. % olivine + clinopyroxene, the magma density was calculated using a melt density of 2,780 kg/m^3 (average from groundmass samples) and observed modal phenocryst proportions ($\rho_{olivine}$=3,400 kg/m^3 (~Fo_{80}) and $\rho_{clinopyroxene}$=3,200 kg/m^3). Plagioclase (due to its density nearly equal to melt density) as well as Fe-Ti oxide and amphibole (due to their small abundances) were considered negligible for these calculations.

2. Construction of the finite element models, loading/unloading conditions and mechanical properties

The finite element models described and discussed in our study were constructed using the commercial software ABAQUS™. The software and the related “Analysis User's

Manual" are available at www.simulia.com. For simplicity, the models are axisymmetric (as shown in Fig. 2a), thus the edifice load was applied as a triangular load using the formulation:

$$L(r) = \rho_v \cdot g \cdot Hi \cdot \left(1 - \frac{r}{R}\right) \qquad \text{(DR1)}$$

where L(r) is the load calculated at the radial coordinate (r), ρ_v is the density of the volcanic material (2,700 kg/m^3), g is the gravitational acceleration (9.81 m/s^2), Hi is the initial height of the edifice (6 km) and R is the radius at the base of the edifice (30 km, cf. Gee et al., 2001). In a second step, we removed 3% of the initial load equivalent to 180 km^3 (see also Table DR2). Both the loading and the unloading step were simulated using the FORTRAN user subroutine *DLOAD in ABAQUS. Far field boundary conditions were applied by means of a set of infinite elements on the right side and at the bottom of the models. The maximum dimension of the elements in the areas of interest for pressure calculations was set to 100 m, as the best compromise between resolution and computational time (Fagan, 1992).

Geometrical parameters Hi and R used to calculate the initial loads for all localities were either collected from literature information or approximated based on analysis of digital elevation models or bathymetric maps (see Table DR2). This procedure, as well as the axial symmetric assumption of the edifices' loads, may have introduced uncertainties in the initial edifice volume estimates. On the other hand, flank collapse volumes considered in this study are well constrained. In our simulations, effects due to collapse are distributed over the entire edifice, while in reality they are likely to concentrate on particular portions of the volcanic system. For example, the effects of the El Golfo debris avalanche were probably much more focused on the El Golfo volcano (~2,000 km^3) than on the whole El Hierro edifice (~5,500 km^3), which would have led to a higher effective unloading fraction on the former. For this reason, the assumption of

75 the unloading volume as portion of the total edifice compensates for the potential error
76 on the estimation of the initial volume.
77 The effects of seawater load and material redistribution due to collapse were tested in
78 separate models not explicitly shown in the main text for the following reasons: (1)
79 Assuming that the seawater load is invariant during the relative time span considered by
80 our models, its simulation does not affect the pressure changes caused by a static flank
81 collapse. (2) In the case of the El Golfo landslide, which is classified as a debris
82 avalanche, the materials are thought to have been redistributed as a relatively thin layer
83 over the seafloor covering an extended area and distances up to 60 km from the edifice
84 (cf. Gee et al., 2001). The latter inclusion in our simulations only slightly decreased the
85 retrieved pressure changes caused by the flank collapse in the area of our main interest,
86 i.e. the magma reservoirs located directly beneath the El Hierro edifice. Thus, the model
87 simplifications shown in the main text of the paper are valid for studying pressure
88 changes at magma chamber levels.
89 **3. Effects of melt % and of different shape of magma reservoir**
90 Numerical models of magma reservoirs commonly consider magma as an
91 incompressible fluid, with bulk modulus varying between 1 and 10 GPa (e.g., Huppert
92 and Woods, 2002; Pinel and Jaupart, 2005). Such assumptions imply that the
93 mechanical behavior of magma reservoirs is dominated by the properties of the melt
94 phase. However, petrological evidence suggests that magma plumbing systems, such as
95 those of e.g. El Hierro (Stroncik et al., 2008) and other Canary Island volcanoes (Klügel
96 et al., 2005; Longpré et al., 2008), as well as Kilauea volcano, Hawaii (Tilling and
97 Dvorack, 1993), may consist of a plexus of dike- and sill-like fractures in the uppermost
98 mantle, where partially crystallized magmas are stored. In our models, we thus consider
99 El Hierro's magma storage zone as a multiphase system, where molten and crystallized

100 material co-exist. From this assumption entails that the storage zone in our models is
101 more compressible than the surrounding rock, in agreement with several independent
102 analyses done on basaltic magmas (e.g., Ryan, 1980 and references therein; Blake,
103 1981).
104 Walsh (1969) derived theoretical relationships for the mechanical properties of a
105 crystal-melt mixture. This study assumes an elastic and isotropic matrix (hereinafter
106 identified by the subscript "c"), specified by its bulk modulus (Kc) and shear modulus
107 (Gc), and an elastic, isotropic and dilute suspension of ellipsoidal melt parcels
108 (hereinafter identified by the subscript "m"), which are characterized by their bulk
109 modulus (Km), shear modulus (Gm) and geometric aspect ratio (minor/major axis
110 herein set to 0.001, cf. Ryan, 1980). The melt parcels decrease the effective elastic
111 response of the basaltic magmas.
112 Since basalts are organized in a millimeter scale, we consider that the assumption of an
113 isotropic elastic behavior for the magmatic reservoir (kilometer scale) as a whole, which
114 is defined by a unique value of "effective" elastic parameters, is reasonable. To
115 calculate the values of effective Young's modulus (E) and effective Poisson's ratio (ν)
116 for the magmatic reservoir used in our modeling, we exploited the following approach.
117 We first fixed the value of Ec=80 GPa and ν=0.25 for fully crystallized basalt (Ryan,
118 1980) and calculated Kc and Gc. In addition, we defined Gm as equal to 0 (fluids do not
119 support shear stresses), and we considered a range for Km between 1 and 10 GPa
120 (Huppert and Woods, 2002; Pinel and Jaupart, 2005). Finally, we calculated the values
121 for the effective E and ν for crystal-melt mixtures (melt % from 0 to 100), using the
122 relationships proposed by Walsh (1969). In Figure DR1-A&B we show the results of
123 these calculations. Depending on the value of Km, hence on the compressibility of the
124 melt phase, the mechanical setups defined by models 1-3 may represent the elastic

response caused by different ranges of melt percentages within the magma reservoir. In Figure DR1-C&D we compare the decompression caused by the El Golfo landslide in a profile beneath the edifice, corresponding to the axis of symmetry of the finite element models, see Fig. 2A of the main text. Clearly, a relative increase of the melt percentage in the storage zone (Figure DR1-D) causes a decrease of its overall elastic stiffness and influences the elastic response of the magmatic reservoir, enhancing the effect of the decompression due to mass unloading.

Furthermore, in Figure DR2 we compare the decompression occurring in a homogeneous half-space with models that consider a range of shapes for the simulated magma storage zone. Oblate-shaped (OS) reservoirs tend to favor slightly higher pressure changes compared with spherical-shaped (SS) or prolate-shaped (PS) reservoirs. However, the general directions of the vectors (i.e. from the bottom to the top of the reservoir) as well as the magnitudes of the differential pressure are largely unaffected.

The assumption of further heterogeneities, as for example a layered lithosphere, might affect the pressure changes at shallow levels but, in our tests, had no major effect on the magma reservoir surroundings. Based on these considerations, we can state that our results give a conservative but realistic representation of static pressure changes caused by surface mass-wasting at the discussed volcanoes.

4. Limitations and validity of the models

High pressures and temperatures, co-existence of several polyphase aggregates, volatiles and fluids add complexity to the analysis of magma reservoir feedback processes using simplified mechanical models. Nevertheless, for short time-scales, we consider the assumption of an elastic regime appropriate, as that of the magma reservoirs as zones of structural weakening causing localization of stresses (Kanamori, 1972; Gudmundsson,

1988). On longer time-scales, viscous effects may also play an important role in determining the amount of stress changes in the magma reservoir surroundings (Newman et al., 2006). Moreover, future studies may refine quantitative evaluations of pressure changes due to volcano flank collapse by adding complexity to the geometries of the volcanic edifices, collapse scars and magma plumbing systems. More complex dynamic modeling and material properties, on the other hand, would allow better assessment of feedback processes caused by the pressure gradients revealed by our simulations. However, we argue that none of these potential improvements would change the principal outcome of our work.

5. Possible effects on melt production at ocean island volcanoes

Differing unloading timescales and geometries for deglaciation (thousands of years, sheet-like) and catastrophic debris avalanches on volcano flanks (minutes to days?, wedge-like) imply different rates and structural patterns in the systems' accommodation to the new stress conditions. In both cases, however, the net stress change, that is decompression, is analogous and useful comparisons can be made with studies that have investigated the effects of deglaciation on Icelandic volcanism. For example, Jull and McKenzie (1996) have shown that ice unloading during deglaciation can cause increased melt production in Iceland's spreading ridge system (see also Maclennan et al., 2002). Using numerical models, these authors found that, despite largest decompression amplitudes just below the ice sheet (ΔP= 20 MPa), the maximum effect on mantle melting was actually much deeper, at a depth of about 80 km. In the presence of both a mantle plume and a spreading ridge, the young Icelandic crust and lithosphere are warmer and more ductile than old oceanic or continental upper mantle. The resulting melting interval is thus thick (about 100 km), from the base of the crust at 20 km depth to the solidus at about 115 km depth.

The Icelandic case therefore differs considerably from pure hot-spot settings without spreading ridge, such as Hawaii or the Canary Islands. There, the older and colder oceanic lithosphere results in a significant mechanical boundary layer. Under these conditions, the melting zone is thinner and restrained at much greater depth, i.e. in the spinel and garnet (mostly) stability fields between about ~70-140 km depth (Watson and McKenzie, 1991; Hoernle and Schmincke, 1993).

The above-mentioned considerations, combined with the results of our numerical models, which imply negligible decompression at depths of magma generation, suggest that the unloading due to large-scale volcano flank collapse is unlikely to cause effects of similar magnitude on ocean islands as has been described for deglaciation periods in Iceland.

6. References cited in the Supplementary Information

Blake, S., 1981, Volcanism and the dynamics of open magma chambers: Nature, v. 289, p. 783–785.

Danyushevsky, L. V., 2001, The effect of small amounts of H_2O on crystallisation of mid-ocean ridge and backarc basin magmas: Journal of Volcanology and Geothermal Research, v. 110, p. 265–280.

Dixon, J.E., Clague, D.A., Wallace, P., and Poreda, R., 1997, Volatiles in alkalic basalts from the North Arch volcanic field, Hawaii: extensive degassing of deep submarine-erupted alkalic series lavas: Journal of Petrology, v. 38, p. 911–939.

Fagan, M. J., 1992, Finite Element Analysis: Theory and Practice: Longman,

Gee, M. J. R., Watts, A. B., Masson, D. G. and Mitchell, N. C., 2001, Landslides and the evolution of El Hierro in the Canary Islands: Marine Geology, v. 177, p. 271–293.

Gudmundsson, A., 1988, Effect of tensile stress concentration around magma chambers on intrusion and extrusion frequencies: Journal of Volcanology and Geothermal Research, v. 35, p. 179–194.

Hoernle, K., and Schmincke, H.-U., 1993, The role of partial melting in the 15-Ma geochemical evolution of Gran Canaria: A blob model for the Canary Hotspot: Journal of Petrology, v. 34, p. 599–626.

Hora, J. M., Singer, B. S. and Wörner G., 2007, Volcano evolution and eruptive flux on the thick crust of the Andean Central Volcanic Zone: 40Ar/39Ar constraints from Volcan Parinacota, Chile: Geological Society of America Bulletin v. 119, p. 343–362.

Huppert, H. E., and Woods, A. W., 2002, The role of volatiles in magma chamber dynamics: Nature, p. 420, v. 493–495.

Kanamori, H., 1972, Relation between tectonic stress, great earthquakes and earthquake swarms: Tectonophysics, v. 14, p. 1–12.

Klügel, A., Hansteen, T. H. and Galipp K., 2005, Magma storage and underplating beneath Cumbre Vieja volcano, La Palma (Canary Islands): Earth and Planetary Science Letters, v. 236, p. 211–226.

Longpré, M., Troll, V. R. and Hansteen T. H., 2008, Upper mantle magma storage and transport under a Canarian shield-volcano, Teno, Tenerife (Spain): Journal of Geophysical Research, v. 113, B-08203.

Maclennan, J. et al., 2002, The link between volcanism and deglaciation in Iceland: Geochemistry Geophysics Geosystems, v. 3, p. 1062.

Newman, A. V., Dixon, T. H. and Gourmelen N., 2006, A four-dimensional

viscoelastic deformation model for Long Valley Caldera, California, between 1995 and 2000: Journal of Volcanology and Geothermal Research, v. 150, p. 244–269.

Patriat, M. et al., 2002, Deep crustal structure of the Tuamotu plateau and Tahiti (French Polynesia) based on seismic refraction data: Geophysical Research Letters, v. 29, p. 1656.

Robinson, J. E., and Eakins, B. W., 2006, Calculated volumes of individual shield volcanoes at the young end of the Hawaiian Ridge: Journal of Volcanology and Geothermal Research, v. 151, p. 309–317.

Schmincke, H.-U., 1998, Gran Canaria: Geological Field Guide, Pluto Press.

Siebert, L., Begöt, J. E. and Glicken H., 1995, The 1883 and late-prehistoric eruptions of Augustine volcano, Alaska: Journal of Volcanology and Geothermal Research, v. 66, p. 367–395.

Spera, F. J., 2000, Physical properties of magma: Encyclopedia of Volcanoes, p. 171–190.

Tilling, R. I., and Dvorak, J. J., 1993, Anatomy of a basaltic volcano: Nature, v. 363, p.125–133.

Voight, B., Glicken, H., Janda, R. and Douglas P., 1981, Catastrophic rockslide avalanche of May 18. In P. W. Lipman and D. R. Mullineaux, The 1980 Eruptions of Mount St. Helens .

Walter, T. R., 2003, Buttressing and fractional spreading of Tenerife, an experimental approach on the formation of rift zones: Geophysical Research Letters, v. 30, p. 1296.

Walsh, J.B., 1969, New analysis of Attenuation in Partially melted rock: Journal of Geophysical Research, v.74, p. 4333-4337.

Watson, S., and McKenzie, D., 1991, Melt generation by plumes: A study of Hawaiian volcanism: Journal of Petrology, v. 32, p. 501–537.

7. Supplementary Tables and Figures:

Table DR1: Outcrop localities investigated on El Hierro Island.

	Latitude (°N)	Longitude (°W)	Altitude (m)	Stratigraphy	Lava Type	Density(kg/m^3)
1	27,73019	18,05931	1382	post-EGL	basalt	–
2	27,73083	18,05921	1381	post-EGL	ankaramite	–
3	27,73133	18,05939	1372	post-EGL	ankaramite	–
4	27,72932	18,05962	1371	post-EGL	basalt	–
5	27,73137	18,05931	1370	post-EGL	ankaramite	–
6	27,73288	18,06004	1368	post-EGL	ankaramite	–
7	27,73246	18,05962	1368	post-EGL	ankaramite	–
8	27,73319	18,06025	1366	post-EGL	ankaramite	–
9	27,73270	18,05985	1365	post-EGL	ankaramite	2970
10	27,73338	18,06026	1361	post-EGL	ankaramite	–
11	27,73227	18,05908	1355	post-EGL	ankaramite	–
12	27,73158	18,05857	1355	post-EGL	ankaramite	–
13	27,73028	18,05850	1347	post-EGL	basalt	2870
14	27,72953	18,05870	1338	post-EGL	basalt	2730
15	27,73271	18,05805	1335	post-EGL	ankaramite	–
16	27,72820	18,05807	1327	post-EGL	basalt	2740
17	27,73317	18,05791	1326	post-EGL	ankaramite	–
18	27,72806	18,05817	1325	post-EGL	basalt	–
19	27,73385	18,05820	1310	post-EGL	ankaramite	–
20	27,72886	18,05250	1262	post-EGL	basalt	2680
21	27,73010	18,05216	1261	post-EGL	basalt	–
22	27,73165	18,05142	1243	post-EGL	basalt	–
23	27,77451	17,94374	1003	post-EGL	basalt	–
24	27,74072	18,05241	934	post-EGL	basalt	–
25	27,73977	18,04936	934	post-EGL	basalt	–
26	27,73937	18,04603	933	post-EGL	basalt	–
27	27,74119	18,05684	895	post-EGL	ankaramite	–
28	27,74164	18,06080	878	post-EGL	ankaramite	–
29	27,74064	18,06523	849	post-EGL	ankaramite	–
30	27,73991	18,03150	847	post-EGL	basalt	–
31	27,73992	18,03151	847	post-EGL	ankaramite	–
32	27,73977	18,02964	832	post-EGL	ankaramite	–
33	27,74014	18,06725	831	post-EGL	ankaramite	–
34	27,73954	18,06931	825	post-EGL	ankaramite	–
35	27,73852	18,07070	810	post-EGL	basalt	–
36	27,73778	18,07189	806	post-EGL	ankaramite	–
37	27,73699	18,07699	801	post-EGL	ankaramite	–
38	27,73689	18,07260	796	post-EGL	ankaramite	–
39	27,73600	18,07367	791	post-EGL	ankaramite	–
40	27,73867	18,02507	785	post-EGL	ankaramite	–
41	27,75332	17,98959	762	post-EGL	basalt	–
42	27,75334	17,98994	745	post-EGL	basalt	–

43	27,75341	17,99020	718	post-EGL	basalt	–
44	27,75354	17,99068	686	post-EGL	basalt	–
45	27,75346	17,99136	650	post-EGL	basalt	–
46	27,75168	17,99258	633	post-EGL	basalt	–
47	27,75229	17,99379	557	post-EGL	basalt	–
48	27,74473	18,02584	540	post-EGL	ankaramite	–
49	27,74486	18,10117	450	post-EGL	basalt	–
50	27,74500	18,10090	430	post-EGL	basalt	–
51	27,75355	18,00350	379	post-EGL	basalt	–
52	27,75127	18,05506	276	post-EGL	ankaramite	2940
53	27,74722	18,08758	264	post-EGL	ankaramite	–
54	27,74695	18,08646	261	post-EGL	ankaramite	–
55	27,74810	18,09251	257	post-EGL	ankaramite	–
56	27,74708	18,08386	257	post-EGL	ankaramite	–
57	27,74709	18,08387	257	post-EGL	plag. basalt	–
58	27,75028	18,06707	256	post-EGL	ankaramite	–
59	27,74660	18,07963	242	post-EGL	ankaramite	2890
60	27,75024	18,06703	241	post-EGL	ankaramite	–
61	27,75052	18,01094	190	post-EGL	aph. basalt	2620
62	27,75223	18,09663	134	post-EGL	basalt	–
63	27,78235	18,00092	44	post-EGL	ankaramite	2910
64	27,75696	18,10941	13	post-EGL	basalt	–
65	27,72587	18,02609	1342	uncertain	aph. basalt	–
66	27,72339	18,03004	1315	uncertain	aph. basalt	–
67	27,72202	18,02584	1269	uncertain	basalt	–
68	27,72195	18,02414	1264	uncertain	aph. basalt	–
69	27,71388	18,01479	1257	uncertain	basalt	–
70	27,72250	18,02218	1252	uncertain	basalt	–
71	27,72443	18,08560	1189	uncertain	ankaramite	–
72	27,72297	18,08508	1147	uncertain	ankaramite	–
73	27,72298	18,08509	1147	uncertain	aph. basalt	–
74	27,71270	18,01911	1121	uncertain	basalt	–
75	27,72532	18,09079	1106	uncertain	aph. basalt	2640
76	27,71311	18,02191	1090	uncertain	basalt	–
77	27,71009	18,02308	1042	uncertain	aph. basalt	–
78	27,72260	18,09134	1025	uncertain	aph. basalt	–
79	27,72261	18,09135	1025	uncertain	ankaramite	2940
80	27,72084	18,08935	1006	uncertain	ankaramite	–
81	27,71295	18,02842	1002	uncertain	basalt	–
82	27,71330	18,03263	970	uncertain	basalt	–
83	27,71888	18,09406	936	uncertain	ankaramite	–
84	27,71889	18,09407	936	uncertain	aph. basalt	–
85	27,71264	18,03741	932	uncertain	aph. basalt	–
86	27,71323	18,03857	928	uncertain	basalt	–
87	27,72066	18,09779	906	uncertain	ankaramite	–
88	27,72067	18,09780	906	uncertain	basalt	–
89	27,72369	18,10361	852	uncertain	basalt	–
90	27,72370	18,10362	852	uncertain	ankaramite	–
91	27,79772	17,96879	829	uncertain	basalt	–
92	27,79773	17,96880	829	uncertain	ankaramite	–

93	27,72468	18,10689	826	uncertain	ankaramite	–
94	27,73771	17,95242	809	uncertain	aph. basalt	–
95	27,69630	18,00453	799	uncertain	aph. basalt	–
96	27,73738	17,95302	798	uncertain	basalt	–
97	27,69747	17,99642	785	uncertain	ankaramite	–
98	27,69651	17,99954	785	uncertain	ankaramite	–
99	27,69670	18,01235	782	uncertain	basalt	–
100	27,73633	17,95210	728	uncertain	basalt	–
101	27,70085	18,02648	712	uncertain	basalt	–
102	27,73576	17,95233	704	uncertain	basalt	–
103	27,72735	18,11848	693	uncertain	aph. basalt	–
104	27,68669	17,98540	674	uncertain	aph. basalt	–
105	27,73526	17,95251	643	uncertain	basalt	–
106	27,68589	17,98722	642	uncertain	ankaramite	–
107	27,68488	17,98928	627	uncertain	basalt	–
108	27,68334	17,99472	576	uncertain	ankaramite	–
109	27,68145	17,99572	551	uncertain	basalt	–
110	27,73410	17,95331	545	uncertain	basalt	–
111	27,81238	17,96622	524	uncertain	ankaramite	–
112	27,68382	18,00867	517	uncertain	basalt	–
113	27,68240	18,00198	514	uncertain	basalt	–
114	27,68235	18,00557	509	uncertain	basalt	–
115	27,73347	17,95434	497	uncertain	basalt	–
116	27,68439	18,01318	490	uncertain	aph. basalt	–
117	27,78937	17,92105	479	uncertain	aph. basalt	–
118	27,68597	18,01764	470	uncertain	basalt	–
119	27,68598	18,01765	470	uncertain	ankaramite	–
120	27,73282	17,95438	449	uncertain	basalt	–
121	27,73791	18,14196	379	uncertain	ankaramite	–
122	27,73163	17,95443	361	uncertain	basalt	–
123	27,74719	18,14456	334	uncertain	ankaramite	–
124	27,72349	18,14470	310	uncertain	aph. basalt	–
125	27,74796	18,14239	307	uncertain	ankaramite	–
126	27,74797	18,14240	307	uncertain	basalt	–
127	27,73107	17,95418	302	uncertain	basalt	–
128	27,75426	18,14399	248	uncertain	ankaramite	2960
129	27,75427	18,14400	248	uncertain	aph. basalt	2590
130	27,72990	17,95430	210	uncertain	aph. basalt	–
131	27,72821	17,95438	174	uncertain	aph. basalt	–
132	27,70738	18,14677	125	uncertain	basalt	2830
133	27,64695	17,99310	115	uncertain	basalt	2850
134	27,75660	18,14840	60	uncertain	ankaramite	3020
135	27,75839	18,14964	33	uncertain	ankaramite	–
136	27,72521	18,05244	1464	pre-EGL	basalt	–
137	27,72566	18,06711	1417	pre-EGL	ankaramite	2890
138	27,72740	18,04769	1407	pre-EGL	basalt	–
139	27,72550	18,04939	1407	pre-EGL	basalt	2870
140	27,72490	18,05349	1392	pre-EGL	plag. basalt	2600
141	27,72490	18,05349	1392	pre-EGL	ankaramite	2880
142	27,72649	18,05597	1346	pre-EGL	plag. basalt	–

143	27,72284	18,05528	1313	pre-EGL	ankaramite	–
144	27,72268	18,06655	1300	pre-EGL	ankaramite	–
145	27,72399	18,07506	1270	pre-EGL	ankaramite	2960
146	27,75856	17,97703	1248	pre-EGL	aph. basalt	2550
147	27,75862	17,97679	1244	pre-EGL	ankaramite	3000
148	27,75862	17,97579	1233	pre-EGL	ankaramite	–
149	27,76259	17,98095	1201	pre-EGL	basalt	–
150	27,76165	17,98055	1167	pre-EGL	aph. basalt	–
151	27,76132	17,98047	1155	pre-EGL	aph. basalt	–
152	27,76138	17,98087	1125	pre-EGL	aph. basalt	–
153	27,76063	17,98067	1109	pre-EGL	aph. basalt	–
154	27,76019	17,98142	1089	pre-EGL	ankaramite	–
155	27,75930	17,98197	1070	pre-EGL	basalt	–
156	27,75878	17,98230	1065	pre-EGL	plag. basalt	–
157	27,75767	17,98235	1046	pre-EGL	plag. basalt	–
158	27,75843	17,98221	1045	pre-EGL	aph. basalt	–
159	27,75697	17,98399	1001	pre-EGL	basalt	–
160	27,77583	17,94294	980	pre-EGL	aph. basalt	2710
161	27,75615	17,98582	966	pre-EGL	ankaramite	–
162	27,77485	17,94344	957	pre-EGL	plag. basalt	–
163	27,77486	17,94345	957	pre-EGL	ankaramite	–
164	27,75604	17,98612	956	pre-EGL	basalt	–
165	27,75573	17,98677	935	pre-EGL	basalt	–
166	27,75554	17,98681	922	pre-EGL	basalt	–
167	27,75554	17,98693	903	pre-EGL	aph. basalt	–
168	27,74435	18,11209	877	pre-EGL	basalt	–
169	27,75517	17,98689	869	pre-EGL	basalt	–
170	27,74401	18,11038	861	pre-EGL	aph. basalt	–
171	27,75428	17,98788	853	pre-EGL	basalt	–
172	27,74349	18,10904	841	pre-EGL	basalt	–
173	27,74313	18,10879	825	pre-EGL	aph. basalt	–
174	27,74275	18,10799	817	pre-EGL	basalt	–
175	27,75403	17,98850	808	pre-EGL	basalt	–
176	27,74276	18,10749	800	pre-EGL	basalt	–
177	27,74277	18,10750	800	pre-EGL	ankaramite	–
178	27,73707	17,95264	780	pre-EGL	ankaramite	–
179	27,74271	18,10605	773	pre-EGL	ankaramite	–
180	27,74239	18,10580	757	pre-EGL	ankaramite	–
181	27,79997	17,97989	755	pre-EGL	ankaramite	3010
182	27,74235	18,10518	743	pre-EGL	ankaramite	–
183	27,80082	17,98013	724	pre-EGL	basalt	2870
184	27,80067	17,98018	723	pre-EGL	ankaramite	–
185	27,80030	17,98034	706	pre-EGL	basalt	–
186	27,79943	17,98073	682	pre-EGL	basalt	–
187	27,74247	18,10239	668	pre-EGL	basalt	–
188	27,80663	17,97708	665	pre-EGL	ankaramite	–
189	27,79930	17,98102	648	pre-EGL	basalt	–
190	27,79931	17,98103	648	pre-EGL	ankaramite	–
191	27,74258	18,10237	645	pre-EGL	ankaramite	–
192	27,75256	17,99162	644	pre-EGL	basalt	–

193	27,75304	17,99124	643	pre-EGL	basalt	–
194	27,79895	17,98110	633	pre-EGL	basalt	–
195	27,74284	18,10129	624	pre-EGL	aph. basalt	–
196	27,75268	18,11980	620	pre-EGL	ankaramite	–
197	27,75269	18,11981	620	pre-EGL	basalt	–
198	27,79840	17,98123	619	pre-EGL	trachyte	2420
199	27,79814	17,98132	607	pre-EGL	aph. basalt	–
200	27,79803	17,98153	590	pre-EGL	plag. basalt	–
201	27,74324	18,10132	583	pre-EGL	ankaramite	–
202	27,79769	17,98152	569	pre-EGL	aph. basalt	–
203	27,74351	18,10128	553	pre-EGL	aph. basalt	–
204	27,79805	17,98188	545	pre-EGL	basalt	–
205	27,79836	17,98198	526	pre-EGL	plag. basalt	–
206	27,79784	17,98216	514	pre-EGL	trachyte	2360
207	27,74410	18,10112	506	pre-EGL	aph. basalt	–
208	27,74411	18,10113	506	pre-EGL	ankaramite	–
209	27,79720	17,97977	500	pre-EGL	aph. basalt	2710
210	27,79819	17,98223	499	pre-EGL	trachyte	–
211	27,79811	17,98249	497	pre-EGL	plag. basalt	–
212	27,74439	18,10109	489	pre-EGL	ankaramite	–
213	27,79774	17,98244	479	pre-EGL	aph. basalt	–
214	27,79754	17,98206	471	pre-EGL	aph. basalt	–
215	27,79728	17,98187	462	pre-EGL	basalt	–
216	27,74485	18,10116	450	pre-EGL	ankaramite	–
217	27,78659	17,92121	448	pre-EGL	ankaramite	2990
218	27,79697	17,98217	443	pre-EGL	basalt	–
219	27,79492	17,98298	434	pre-EGL	aph. basalt	–
220	27,79567	17,98277	433	pre-EGL	basalt	–
221	27,74499	18,10089	430	pre-EGL	ankaramite	–
222	27,79469	17,98311	429	pre-EGL	aph. basalt	–
223	27,79436	17,98340	419	pre-EGL	ankaramite	–
224	27,79437	17,98341	419	pre-EGL	basalt	–
225	27,79379	17,98363	404	pre-EGL	basalt	–
226	27,79322	17,98389	395	pre-EGL	basalt	–
227	27,79236	17,98451	379	pre-EGL	basalt	–
228	27,79186	17,98471	369	pre-EGL	basalt	–
229	27,79141	17,98510	360	pre-EGL	basalt	–
230	27,79142	17,98532	354	pre-EGL	aph. basalt	–
231	27,79138	17,98556	336	pre-EGL	aph. basalt	–
232	27,79140	17,98573	326	pre-EGL	aph. basalt	–
233	27,79116	17,98613	307	pre-EGL	basalt	–
234	27,79060	17,98666	295	pre-EGL	basalt	–
235	27,78988	17,98464	290	pre-EGL	aph. basalt	2720
236	27,79080	17,98679	279	pre-EGL	ankaramite	–
237	27,79081	17,98680	279	pre-EGL	basalt	–
238	27,79071	17,98704	249	pre-EGL	basalt	–
239	27,79025	17,98746	231	pre-EGL	basalt	–
240	27,78985	17,98797	219	pre-EGL	aph. basalt	–
241	27,78944	17,98846	211	pre-EGL	basalt	–
242	27,78928	17,98900	179	pre-EGL	ankaramite	–

243	27,76695	17,91809	160	pre-EGL	aph. basalt	2700
244	27,78864	17,98902	158	pre-EGL	basalt	–

Lava types are divided into four categories, according to modal mineralogy: 1) aphyric to sub-aphyric (<5 vol. % phenocrysts of olivine/clinopyroxene/plagioclase, called aphyric basalt); 2) plagioclase-phyric (5-40 vol. %, called plagioclase basalt, which is sometimes referred to as “trachytes” in the literature); 3) moderately olivine- and/or clinopyroxene-phyric (5-20 vol. %, called basalt) and 4) highly olivine-clinopyroxene-phyric (>20 vol. %, called ankaramites). In Figure 1, the first three types are encompassed under the “crystal-poor” category. Where available, stratigraphic position and calculated magma density is also given.

Table DR2: Geometrical parameters used for the finite element simulations of conical edifices that experienced a volcano flank collapse.

	Height [km]	Radius [km]	Edifice Volume [km^3]	Collapse Volume [km^3]	% initial load
Augustine	~1.2 [a]	3.2(*)	13 [a]	0.3 [a]	0.4%
St. Helens	1(*)	6(*)	38 [b]	2.5 [c]	6.5%
Parinacota	1.5(*)	5.5(*)	45 [d]	6 [d]	13%
Teno	5.3 [e]	25 [e]	3,500(*)	~50 [f]	1,4%
El Golfo	6 [g]	30 [g]	5,500 [h]	~180 [f]	3%
Tahiti-Nui	4 [i]	50 [i]	10,500(*)	~1,150 [j]	7%
Waianae	~6(*)	63(*)	25,000 [k]	~6,100 [l]	38%

(a) Siebert et al. (1995); (b) Voight et al. (1981); (c) McGuire (1996); (d) Hora et al. (2007) ; (e) Walter (2003) ; (f) Masson et al. (2002) ; (g) Gee et al. (2001); (h) Schmincke (1998) ; (i) Patriat et al. (2002) ; (j) Hildenbrand et al. (2004) ; (k) Robinson and Eakins (2006) ; (l) Presley et al. (1997) .

(*) Other values have been either calculated from other known parameters or estimated from digital elevation models and bathymetric maps.

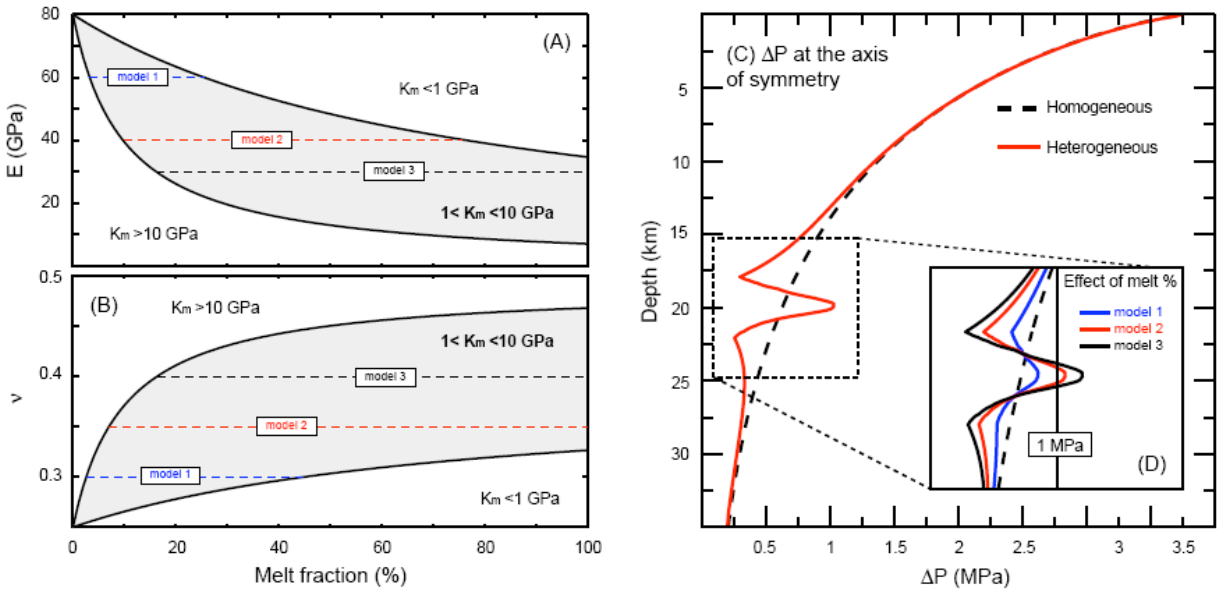

Figure DR1: Effect of melt %. (A & B) Effective elastic properties defined by Young's moduli (E) and Poisson's ratios (ν) calculated using the theoretical relationships of Walsh (1969) for melt fractions varying from 0 to 100% within the magma storage zone. See section 3 for details of the calculations. (C) Decompression amplitudes caused by the El Golfo landslide calculated on the axis of symmetry of the FE models (see Fig. 2A of the main text). Results for homogeneous (dashed line) and heterogeneous (solid red line) models are compared. (D) Melt percentage within the magma storage zone significantly affects the mechanical response of the surrounding rock. "Model 2" corresponds to the mechanical setup used for the finite element models that are presented in the main text.

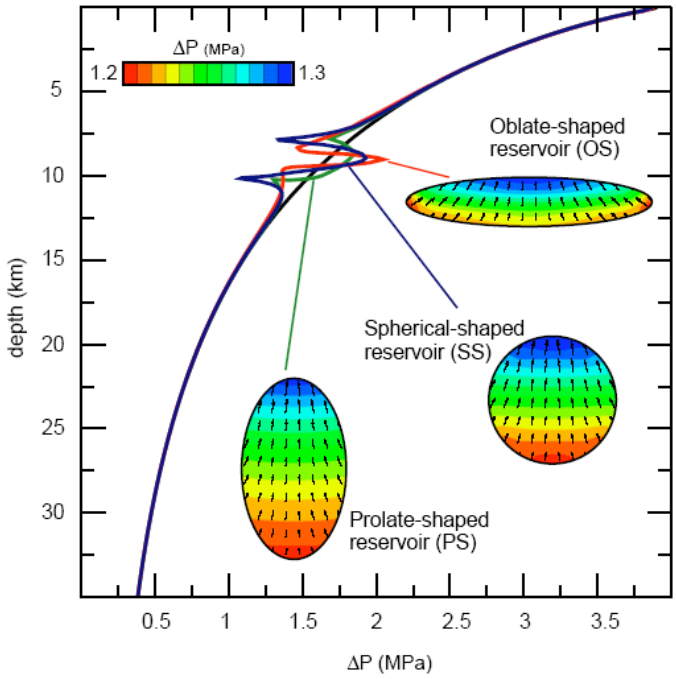

Figure DR2: Effect of shape of magma storage zone on landslide-induced decompression.